(Received 20 May 2025, Accepted 1 July 2025, Scheduled 18 July 2025)

A Low-Profile Implantable Antenna with Enhanced Performance for 2.45 GHz NFC-Based Healthcare Systems

Emtiaz Ahmed Mainul* and Md. Faruque Hossain

Department of Electronics and Communication Engineering, Khulna University of Engineering & Technology Khulna-9203, Bangladesh

ABSTRACT: This work presents a compact single-band patch antenna designed for Near-Field Communication (NFC) based skin implant applications. The antenna features an inset-fed patch structure on an FR-4 substrate and resonates at 2450 MHz. Three techniques are employed to miniaturize the antenna: a shorting pin between the patch and ground, defected ground structure (DGS), and utilization of tissue electrical properties. A polyamide insulator is used to cover the antenna for biocompatibility. Thus, the optimized antenna volume is found to be $6 \times 6 \times 0.46\,\text{mm}^3$, with near-perfect impedance matching of $51.14 + j4.6\Omega$. The antenna also offers enhanced impedance bandwidths of 52.24%. Compared to state-of-the-art designs, the proposed antenna exhibits significantly reduced specific absorption rate (SAR) values of 1.32 W/kg and 0.152 W/kg averaged over 1 g and 10 g of tissue, respectively, in compliance with international safety guidelines. The proposed antenna is effectively free from gain limitations due to the inherently short communication range of NFC technology. Finally, the antenna is measured for its return loss ex vivo, and it is found to be in close agreement with the simulation results. Thus, the balanced performance among the compact size, large bandwidth, and very low SAR makes the antenna a strong candidate for NFC based healthcare systems.

1. INTRODUCTION

The rapid advancement of wireless biomedical telemetry systems has underscored the importance of implantable antennas that can operate reliably within the human body for applications such as medical monitoring, neural stimulation, cardiac rhythm management, and drug delivery. These systems rely on efficient electromagnetic coupling between implanted devices and external readers. Due to the inherently lossy and heterogeneous nature of biological tissues, implantable antennas must be carefully engineered to ensure compact form factors, biocompatibility, impedance stability, low power consumption, and compliance with electromagnetic safety regulations [1–6].

The selection of the operating frequency is critical in implantable antenna design, as it influences both antenna size and communication performance. Low-frequency bands offer better tissue penetration but necessitate larger antennas, while high-frequency bands support miniaturization but experience increased attenuation due to the lossy and dispersive nature of biological tissues [7]. These constraints reduce the effectiveness of far-field communication (FFC) in implantable systems. Near-Field Communication (NFC) presents a viable alternative by leveraging inductive magnetic coupling to enable efficient short-range energy transfer and data communication through tissue, thereby supporting compact and low-power designs. In NFC-based systems, wearable medical devices (WMDs) are strategically employed as external relays to capture the weakened signals emitted by implantable medical devices (IMDs) and retransmit them to external receivers [8–11]. This relay-assisted communication architecture reduces the transmitting power required by IMDs, thereby minimizing localized electromagnetic (EM) absorption and ensuring compliance with specific absorption rate (SAR) safety thresholds. Furthermore, by lowering power consumption, this approach significantly improves the energy efficiency and operational longevity of battery-powered IMDs, making it a vital aspect of safe and sustainable implantable communication system design. An overview of the NFC-based healthcare system is illustrated in Fig. 1.

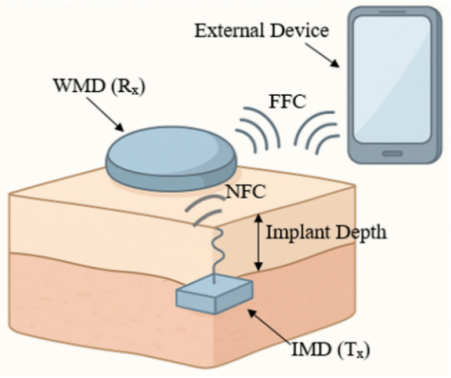

FIGURE 1. Overview of NFC-based health care system.

The selection of substrate and superstrate materials plays a pivotal role in implantable antenna design, as these materials critically influence key performance metrics, biocompatibility, and patient safety. Substrates with a high dielectric constant are particularly advantageous for miniaturization, enabling com-

* Corresponding author: Emtiaz Ahmed Mainul (emtiaz.mainul@gmail.com).

TABLE 1. Performance comparison among some recent literatures.

Ref./year	Tissue	Freq. (GHz)	Antenna Volume (mm^3)	FBW (%)	SAR (W/kg)	
					1 g	10 g
[21]/2022	Skin	2.45	$8 \times 17 \times 3.7$	15.1	464.72	160.81
[22]/2023	Skin	0.400	$17.2 \times 14.8 \times 0.254$	5.75	-	-
		2.45		7.76		
[23] /2023	Skin	2.45	$21 \times 13.5 \times 0.254$	47.7	0.78	-
[24]/2024	Skin	5.8	$7 \times 15 \times 0.3$	0.004	0.28	-
[25]/2024	Skin	402	$12.5 \times 12.5 \times 0.254$	33.33	610	-
[26] /2024	Skin	2.45	$15.5 \times 9 \times 1.27$	30.67	368	45.2
[9] /2025	Skin	2.41	$5 \times 5 \times 1.016$	16.8	767	91.1
		5.81		22.5	774	90.8
This Work	**Skin**	**2.45**	$\mathbf{6 \times 6 \times 0.46}$	**52.24**	**1.32**	**0.152**

pact antenna geometries by shortening the guided wavelength. However, these substrates must also exhibit a low loss tangent ($\tan\delta$) to minimize dielectric losses and reduce unwanted energy dissipation within biological tissues. While flexible substrate materials have garnered attention in recent years for their conformal integration with soft tissues, they often suffer from low dielectric constants, increased fabrication complexity, elevated SAR levels, and performance degradation under mechanical deformation [12]. In contrast, rigid substrates provide higher dielectric constants — crucial for antenna miniaturization — along with enhanced mechanical stability and precise manufacturability. Consistent with previous studies [13–15], FR-4 was selected in this work due to its low cost, ease of fabrication, and ready availability in our laboratory. To ensure biocompatibility and prevent inflammatory or cytotoxic responses upon implantation, a biocompatible superstrate layer is required to encapsulate the antenna. Notably, the dielectric properties and physical thickness of the superstrate substantially influence the radiation efficiency and field distribution of the antenna, thereby impacting SAR levels within adjacent tissues [7].

Miniaturization remains a significant challenge due to the electromagnetic constraints imposed by the implant environment and tissue absorption. Various techniques have been explored to address this, including meandering slots, high-permittivity substrates, shorting pins, and defected ground structures (DGSs) [16, 17]. Lengthening the current path within the patch structure via meandered or spiral geometries is among the most common methods to reduce antenna size while maintaining acceptable performance [18]. However, miniaturization typically results in trade-offs such as reduced bandwidth and gain, along with increased resistive losses caused by the surrounding biological tissues [15]. To mitigate these drawbacks, methods like using parasitic elements or metamaterial-inspired structures have been investigated to enhance gain and bandwidth, although they may introduce fabrication complexity or size increases [19, 20].

Several recently reported implantable antenna designs have demonstrated varying levels of performance in terms of size, bandwidth, gain, and SAR. The antenna in [21] operated at 2.45 GHz with a relatively large volume of $8\times17\times3.7\,mm^3$, offering a moderate bandwidth of 15.1%, but exhibited extremely high SAR values of 464.72 W/kg (1 g) and 160.81 W/kg (10 g), which far exceed safety limits. Following that, a large and thin antenna ($17.2 \times 14.8 \times 0.254\,mm^3$) was designed for 400 MHz and 2.45 GHz, achieving narrow bandwidths of 5.75% and 7.76%, respectively, and a very low gain of -42.97 dBi at 400 MHz, limiting its practical usability [22]. After that, the design in [23] employed large antenna dimensions of $21 \times 13.5 \times 0.254\,mm^3$ and achieved a wider bandwidth of 47.7% at 2.45 GHz but still reported a relatively low gain of -15.8 dBi and a better SAR of 0.78 W/kg for the 1 g standard. Moving forward, an antenna with dimensions of $7 \times 15 \times 0.3\,mm^3$ exhibited a severely limited bandwidth of only 0.004% at the 5.8 GHz band, although the SAR was relatively low at 0.28 W/kg for the 1 g standard [24]. Another design in [25] targeted 402 MHz with an antenna volume of $12.5 \times 12.5 \times 0.254\,mm^3$ and achieved a 33.33% bandwidth but exhibited an extremely high SAR of 610 W/kg for the 1 g standard. Moreover, an antenna with a volume of $15.5 \times 9 \times 1.27\,mm^3$ achieved a bandwidth of 30.67% and a gain of -28.3 dBi at 2.45 GHz; however, it also resulted in significantly high SAR values of 368 W/kg (1 g) and 45.2 W/kg (10 g) [26]. The multi-band antenna in [9], designed for 2.41 GHz and 5.81 GHz with a volume of $5 \times 5 \times 1.016\,mm^3$, achieved bandwidths of 16.8% and 22.5%, respectively, but showed extremely high SAR levels of up to 767 W/kg (1 g) and 774 W/kg (1 g). Compared to these designs, the proposed antenna in this work offers a compact size of $6 \times 6 \times 0.46\,mm^3$, a significantly wider bandwidth of approximately 1280 MHz (~52.24%), and SAR values of only 1.32 W/kg (1 g) and 0.152 W/kg (10 g), well within the international safety guidelines, as detailed in Table 1. These results highlight the superior balance of miniaturization, bandwidth, and safety achieved by the proposed antenna.

As gain is often a concern in implantable antenna designs, the proposed antenna is effectively free from gain limitations due to the inherently short communication range of NFC technology. This enables the antenna to prioritize miniaturization, bandwidth, and safety without compromising overall system performance. In this work, a novel skin-implantable antenna is proposed by integrating an inset-fed patch, a defected ground

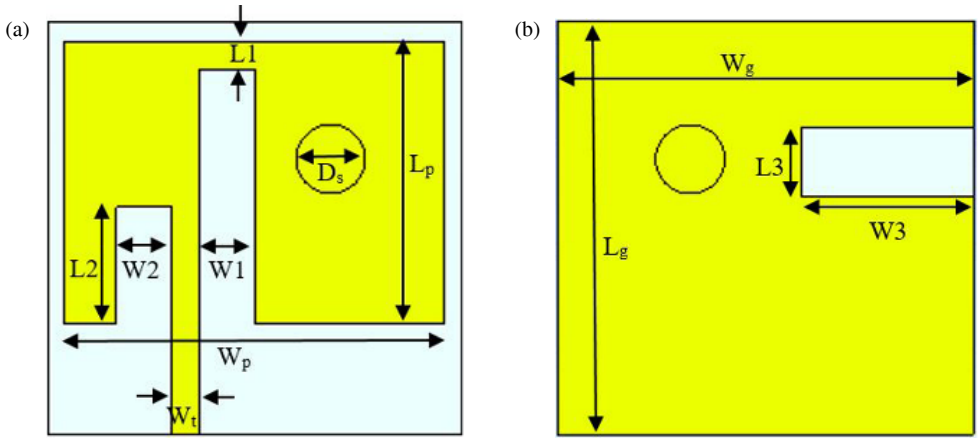

FIGURE 2. Proposed antenna: (a) radiating patch and (b) defected ground structure (DGS).

structure (DGS), and a shorting pin. These elements collectively contribute to miniaturization ($6 \times 6 \times 0.46\,\text{mm}^3$) and single-band functionality at 2.45 GHz. Near-perfect impedance matching is achieved with values of $51.14 + j4.6\Omega$ at 2.45 GHz, as confirmed through $|S_{11}|$ responses simulated in Computer Simulation Technology (CST) and validated via the antenna's equivalent circuit in Advanced Design System (ADS). The antenna exhibits a wide bandwidth of approximately 1280 MHz around the 2.45 GHz band, providing coverage well beyond the 2.4–2.48 GHz Industrial, Scientific, and Medical (ISM) band required for reliable NFC communication. Specific Absorption Rate (SAR) analysis reveals reduced values of 1.32 W/kg and 0.152 W/kg for the 1 g and 10 g standards, respectively, well below the international safety limits, ensuring safe operation when being implanted. Performance was evaluated across three demographic categories at a constant implant depth of 4 mm. While resonance frequencies exhibited minor shifts due to age-dependent changes in skin permittivity and conductivity, the bandwidth remained consistently broad and sufficient for effective data transmission across all groups. The proposed antenna is compared with some recent relevant works, which demonstrates superior performance in miniaturization, bandwidth, and SAR compared to most recently published skin-implantable antenna designs. The entire design was conducted using CST Microwave Studio and validated through ex vivo measurements of return loss. The detailed study is organized as follows. Section 2 describes the design methodology and development steps. Section 3 presents the antenna performance analysis, and Section 4 concludes the work and suggests future research directions.

2. DESIGN METHODOLOGY

2.1. Proposed Antenna Structure

The proposed antenna is a rectangular, inset-fed patch whose radiating element consists of two side arms joined by a central vertical segment of length L_1, as shown in Fig. 2(a). The inset feed line creates two gaps: on the right, a gap of width W_1 separates the left arm from the feed, and on the left, a gap of width W_2 separates the right arm. In this design, the right-side gap extends nearly to the top of the patch, where the two arms meet over the length L_1, maximizing the effective current path. The right arm is then shorted to the ground plane via a metallized via of diameter D_s, which provides additional inductive loading for miniaturization. Beneath the patch, as shown in Fig. 2(b), the ground plane incorporates a defected ground structure (DGS) formed by a rectangular slot of length L_3 and width W_3; this DGS further perturbs the ground currents to lower the resonant frequency and improve impedance matching. The overall dimensions of the antenna are defined by the width (W_g) and length (L_g) of the ground plane, which serve as the substrate's boundaries. A 50 Ω inset-fed transmission line of width W_t is used to excite the patch. To ensure biocompatibility, a thin (0.05 mm) polyimide superstrate ($\varepsilon = 4.3$, $\tan\delta = 0.004$) matching the size of the substrate is placed over both the patch and ground [7, 15]. This encapsulation allows safe operation in biological environments. The complete antenna structure has a compact total volume of $6 \times 6 \times 0.46\,\text{mm}^3$ (width × length × total thickness). Together, these geometric parameters define the antenna's compact footprint and its tuned resonance at 2.45 GHz under skin-loading conditions. The detailed geometric parameters are listed in Table 2.

TABLE 2. Antenna parameters.

Parameter	Value (mm)	Parameter	Value (mm)
L_1	0.4	W_p	5.5
L_2	1.7	L_p	4.1
W_1	0.8	W_g	6
W_2	0.8	L_g	6
L_3	1	D_s	0.5
W_3	2.5	W_t	0.4

2.2. Phantom Model

In this study, a simplified single-layer human skin phantom was selected for simulation purposes. The proposed antenna was positioned at a depth of 4 mm within this model, as illustrated in Fig. 3. The dimensions of the phantom were set to

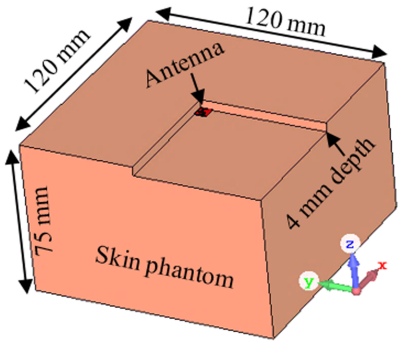

FIGURE 3. Skin phantom ($120 \times 120 \times 75\,\text{mm}^3$) used to simulate the performance of implant antenna.

$120 \times 120 \times 75\,\text{mm}^3$, which is sufficiently large to ensure that the simulation results remain insensitive to boundary effects within the analysis domain. The electrical properties of the skin tissue, specifically the relative permittivity and conductivity at 2.45 GHz, were obtained from [4]. Unless otherwise stated, all dimensions mentioned throughout this paper are in millimeters.

2.3. Development Steps

The mathematical modeling developed in this work captures how the antenna's geometric and material characteristics collectively influence its resonant behavior. The initial design began with a conventional rectangle-shaped microstrip patch antenna based on the transmission line model. This baseline antenna operated at 2.45 GHz under free-space conditions but had a relatively large size of $37.58 \times 29.47 \times 0.39\,\text{mm}^3$. To evaluate its performance in realistic conditions, the antenna was implanted at a 4 mm depth within a skin phantom. A series of miniaturization steps were then implemented, with the antenna remaining under skin-loading conditions throughout the process. The four major development stages of the proposed antenna are illustrated in Figs. 4(a)–(d), and their corresponding performance is compared in Fig. 5.

The miniaturized patch antenna resonates when its effective electrical length (L_{eff}) equals half the guided wavelength [27], expressed as:

$$f_r = \frac{c}{2L_{eff}\sqrt{\varepsilon_{eff}}} \tag{1}$$

To account for both the substrate and surrounding tissue, the effective permittivity (ε_{eff}) is computed using a geometry-dependent weighting factor (β). This linear mixing rule is a first-order effective medium approximation derived from classical mixing formulas [28]. Thus, the effective permittivity can be expressed as:

$$\varepsilon_{eff} = \beta\varepsilon_r^{subs} + (1-\beta)\varepsilon_r^{tissue}(f) \tag{2}$$

where ε_r^{subs} is the relative permittivity of the substrate, and ε_r^{tissue} is the frequency-dependent relative permittivity of skin tissue, typically obtained from the Cole-Cole model.

The initial antenna structure, shown in Fig. 4(a), consisted of a conventional inset-fed rectangular microstrip patch with a solid ground plane. However, this structure failed to exhibit effective resonance under skin-loading conditions due to the altered dielectric environment.

In the second step, shown in Fig. 4(b), a shorting pin was added between the right patch arm and ground plane. This introduced inductive loading, which reduced the effective resonant length and thereby supported further miniaturization. The inductance introduced by the metallic via was estimated using the classical approximation [29], expressed as:

$$L_v = \frac{\mu_0 h}{2\pi}\ln\left(\frac{4h}{D_s}\right) \tag{3}$$

where h is the substrate thickness, D_s the diameter of the shorting via, and μ_0 the permeability of free space. This configuration yielded a partial resonance at 4.37 GHz with a $|S_{11}|$ of -7.35 dB (Fig. 5).

In the third step [Fig. 4(c)], the vertical slot length between the transmission line and right patch arms was increased. This modification extended the current path and increased the effective electrical length L_{eff}, thereby lowering the resonant frequency to 2.85 GHz and significantly improving the $|S_{11}|$ to -17.98 dB (Fig. 5).

In the final step, illustrated in Fig. 4(d), a rectangular defected ground structure (DGS) was etched into the right-hand edge of the ground plane. The DGS perturbs the surface current distribution and controls the guided wave. This resulted in further lowering the resonant frequency and enhanced impedance matching. The impedance, $Z_{DGS}(f)$, introduced by the DGS can be modeled as a parallel combination of a capacitor (C_{DGS}) and an inductor (L_{DGS}) as follows:

$$Z_{DGS}(f) = \frac{1}{j\omega C_{DGS}} \| j\omega L_{DGS} \tag{4}$$

where ω is the angular frequency, and j is the imaginary unit. By incorporating the effects of the antenna geometry, shorting pin, and DGS, the overall resonant condition of the antenna can be approximated as:

$$f_r = \frac{1}{2L_{eff}\sqrt{\varepsilon_{eff}}} - \Delta f_{via} - \Delta f_{DGS} \tag{5}$$

where Δf_{via} represents the frequency shift due to inductive loading from the shorting pin, and Δf_{DGS} represents the shift caused by the DGS-induced parallel LC effect. This final structure achieved the desired resonance at 2.45 GHz with an $|S_{11}|$ of -26.59 dB, as shown in Fig. 5. Besides, the optimized antenna got an impedance of $51.14 + j4.6\,\Omega$ at 2.45 GHz in CST simulation (Fig. 6). It is demonstrated that the co-optimization of geometric and reactive elements successfully resulted in a compact, efficient, and tissue-compliant implantable antenna.

2.4. Antenna Equivalent Circuit

An equivalent circuit model of the proposed inset-fed patch antenna was developed to validate its resonance and impedance behavior. The antenna comprises left and right arms positioned on either side of the transmission line. This physical topology is replicated in the equivalent circuit using lumped elements and simulated in Advanced Design System (ADS), as shown in Fig. 7. The input port (Z_{in}) is matched to $50\,\Omega$ to ensure

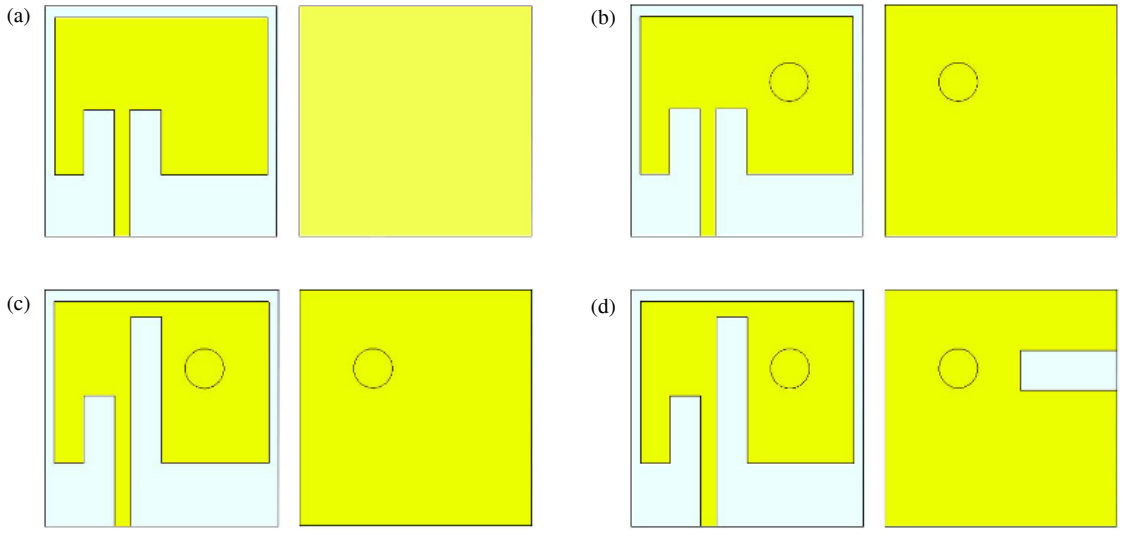

FIGURE 4. Development stages of the proposed antenna design. (a) Step 1. (b) Step 2. (c) Step 3. (d) Step 4.

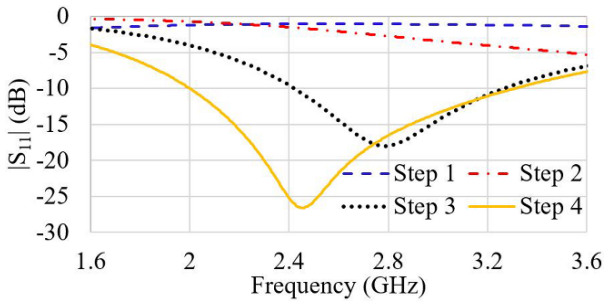

FIGURE 5. Stepwise performance comparison of four antennas (four steps).

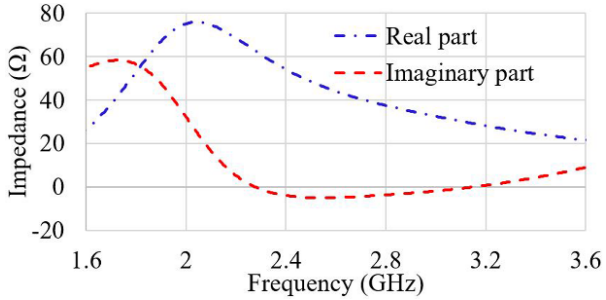

FIGURE 6. Impedance response of the proposed antenna as a function of frequency.

efficient power transfer. The feed line is modeled using a series L_tC_t branch, representing the transmission line. The right and left arms of the patch are modeled as parallel LC networks (L_rC_r and L_lC_l), both connected to the same node at the top of the patch. The right arm is shorted to the ground plane through a shorting pin, which is modeled as an inductor (L_s). This shorting path is connected in series with a defected ground structure (DGS), represented as a parallel L_dC_d circuit, and the entire branch terminates at ground. This configuration captures the coupling effects among the patch, shorting pin, and DGS, all of which influence the antenna's impedance characteristics

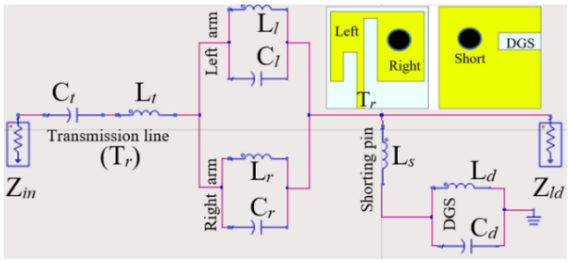

FIGURE 7. Equivalent circuit model of the proposed antenna.

and resonance behavior. Finally, the load impedance (Z_{ld}) of the equivalent circuit is set to 50 Ω to emulate radiation into space, aligning with the impedance observed in Fig. 6 with values of $51.14 + j4.6\,\Omega$ at 2.45 GHz in CST simulations. Although the L_tC_t branch of the transmission line feed serves as the primary resonator near the 2.45 GHz band, the additional structures — namely the left and right arms, shorting pin, and defected ground structure (DGS) — play critical roles in fine-tuning and stabilizing the antenna's performance under skin implantation conditions. The detailed component values are listed in Table 3. As illustrated in Fig. 8, the close match of $|S_{11}|$ responses between the EM (electromagnetic) model in CST and the circuit model in ADS effectively represents the antenna's resonance and impedance characteristics in skin implant conditions.

TABLE 3. Equivalent circuit parameters (units = nH, pF).

Parameter	Value	Parameter	Value
L_p	3.35	C_l	3
C_p	1.25	L_d	6.1
L_r	5	C_d	5.2
C_r	4.5	L_s	11
L_l	4	-	-

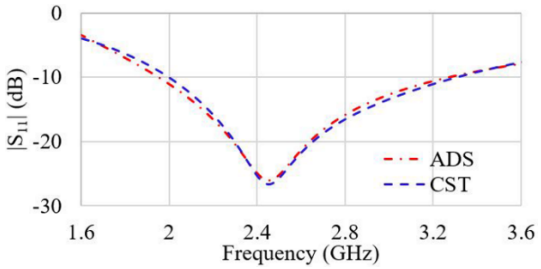

FIGURE 8. Comparison of the simulated $|S_{11}|$ parameter obtained from CST and ADS.

3. RESULTS AND DISCUSSIONS

3.1. Analysis of Simulation Results

3.1.1. Analysis with IMD

The implantable medical device (IMD) was encapsulated using a polyamide casing, which serves as a biocompatible protective layer to isolate the internal components from the surrounding biological environment. The casing encloses essential subsystems, including the implantable antenna, electronics package, sensor modules, battery unit, and power management circuitry, as depicted in Fig. 9(a). To maintain structural compactness and consistent electromagnetic behavior, the casing width was matched to the antenna width, ensuring uniform field distribution across the antenna aperture. The casing height was selected in the range of 4–8 mm, while the length was varied between 10 and 14 mm that are considered moderate and comparable to those used in previous works [30, 31].

To assess the impact of the casing and internal electronics on antenna performance, a perfect electric conductor (PEC) model was used to represent the circuit region during simulation. This approach enabled a comparative analysis with and without the presence of internal circuitry. As shown in Fig. 9(b), variations in the casing height and length had minimal effect on the return loss when the PEC-modeled circuit was included. However, slightly improved impedance matching was observed when the antenna was simulated without internal circuitry, although the resonance frequency remained nearly identical in both cases. These results suggest that the circuit-loaded casing introduces minor impedance variations but does not significantly degrade the antenna's resonance behavior.

3.1.2. Analysis with Three Age Groups

Human skin undergoes physiological changes across different age groups, altering the dielectric properties of the tissue and consequently impacting the performance of implantable antennas. To assess the robustness of the proposed antenna under such variations, simulations were conducted for three demographic categories: average children (age $>$ 5 years), average adults (age $>$ 25 years), and average elderly individuals (age $>$ 60 years). The electrical properties of skin at 2.45 GHz for the adult group served as the reference, as listed in Table 4. Adjusted skin parameters for child and elderly groups were listed in Table 5 based on physiological differences reported in the literature [32–34].

TABLE 4. Electrical properties of human skin for average adults (age $>$ 25 years) [4].

Freq. (MHz)	Permittivity	Conductivity (S/m)
2450	37.88	1.44

Antenna performance was then evaluated across these age groups at a constant implant depth of 4 mm. As shown in Fig. 10, the resonance frequencies slightly varied among the demographic groups due to the age-dependent changes in skin permittivity and conductivity. However, the resonance bandwidths in all cases remained within the 2.4–2.48 GHz ISM band, demonstrating the proposed antenna's ability to maintain operational reliability across different physiological conditions. Although minor shifts in impedance matching and resonant points were observed, the antenna consistently provided sufficient bandwidth for effective data communication across all age categories, highlighting its robust design for diverse user populations.

3.1.3. Influence of Implant Depth (ID)

The effect of varying implant depth on the performance of the proposed antenna was also evaluated. Simulations were conducted for implant depths ranging from 2 mm to 8 mm, representing realistic implantation conditions. As illustrated in Fig. 11, while the return loss profiles exhibited variations in magnitude due to changes in the surrounding dielectric loading, the resonance frequencies consistently remained within the 2.4–2.48 GHz ISM band. This demonstrates the robustness of the antenna's design, ensuring reliable operation across a range of implantation depths. Such stability is crucial for biomedical applications where slight variations in implant positioning may occur due to anatomical differences or surgical limitations.

3.1.4. Effect of Shorting Pin

A parametric analysis was carried out to determine the optimal position of the shorting pin. Considering the geometry of the inset-fed transmission line and defected ground structure (DGS), the shorting pin was placed at four different coordinates: $(x, y) = (-1.1, 1)$, $(1.1, 1)$, $(-2.1, -1)$, and $(-2.1, 2)$. As illustrated in Fig. 12(a), the optimum performance was observed when the shorting pin was positioned at $(x, y) = (1.1, 1)$, because it provided better impedance matching and stable resonance characteristics. This analysis highlights the sensitivity of the antenna's performance to the precise placement of the shorting pin.

Since the proposed antenna is designed for single-band operation, a parametric analysis was conducted to evaluate the influence of the shorting pin's diameter on antenna performance. As shown in Fig. 12(b), varying the diameter from 0.3 mm to 0.7 mm had minimal impact on the resonance frequency, which remained consistently within the targeted ISM band. However, noticeable variations in return loss were observed across the range of diameters. This indicates that while the resonance is largely unaffected by the shorting pin's diameter, its impedance

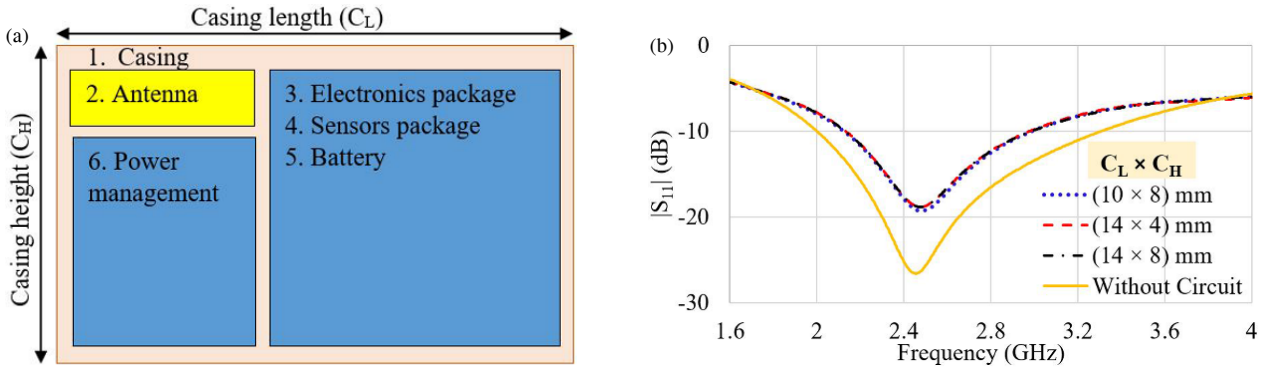

FIGURE 9. (a) IMD structure for NFC applications, and (b) simulated $|S_{11}|$ for different sizes ($C_L \times C_H$) of the IMD system.

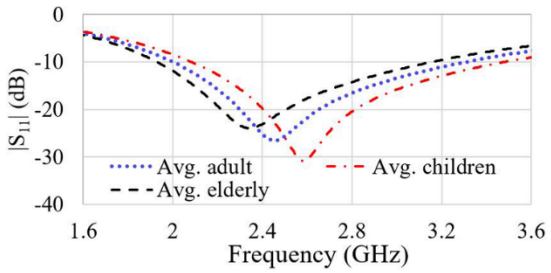

FIGURE 10. Investigation of $|S_{11}|$ for the variation of tissue properties among three age groups.

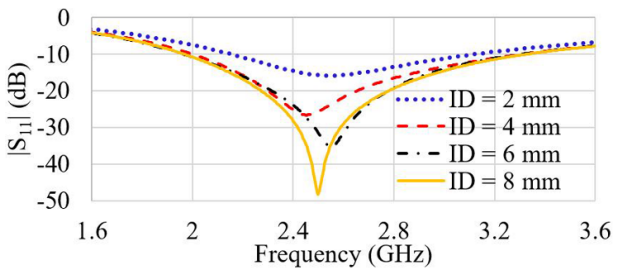

FIGURE 11. Effect of implant depth variation on $|S_{11}|$ performance.

TABLE 5. Electrical properties of human skin for average children and elderly individuals.

Age group	Average children (age > 5 years)	Average elderly (age > 60 years)	**Cause of adjustment**
$\varepsilon_{adjusted}$	$37.88 \times 0.89 \approx 33.69$	$37.88 \times 1.12 \approx 42.18$	Children have a thinner epidermal layer compared to adults due to ongoing growth and development, which can potentially lead to increased skin hydration and blood flow [32–34].
$\sigma_{adjusted}$ (S/m)	$1.44 \times 1.1 \approx 1.584$	$1.44 \times 0.9 \approx 1.29$	The elderly have thinner dermis and epidermis layers compared to adults due to age-related changes in skin structure, potentially resulting in increased water content [32, 34].

matching is sensitive to this parameter, highlighting the importance of maintaining optimal pin dimensions for efficient antenna performance.

3.1.5. Parametric Analysis

A parametric analysis was also carried out to evaluate the fabrication tolerance of the proposed antenna. The analysis focused on the critical structural dimensions of the patch, specifically the lengths (L_1, L_2) and widths (W_1, W_2) of the patch. These parameters were varied incrementally in three steps, with each step measuring approximately 0.2 mm, depending on the specific arm's size. The impact of these variations on the antenna's reflection coefficient is presented in Figs. 13(a)–(d). The results indicate that the resonance frequencies undergo minimal shifts, demonstrating the antenna's robustness against dimensional variations. Moreover, the bandwidth of each resonant mode remains consistently within the designated frequency bands, confirming that the antenna can reliably operate even with slight dimensional deviations during fabrication. Since the antenna utilizes a DGS, a parametric analysis was also conducted on the dimensions of the DGS to assess its influence on antenna performance.

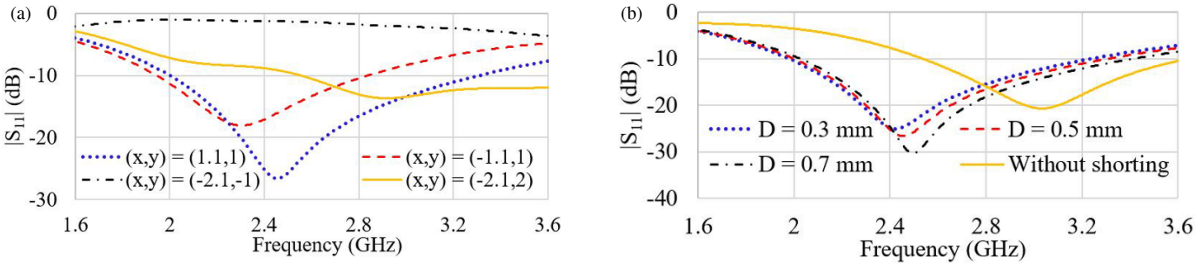

FIGURE 12. Simulated $|S_{11}|$ for (a) different positions, and (b) different diameters of the shorting pin.

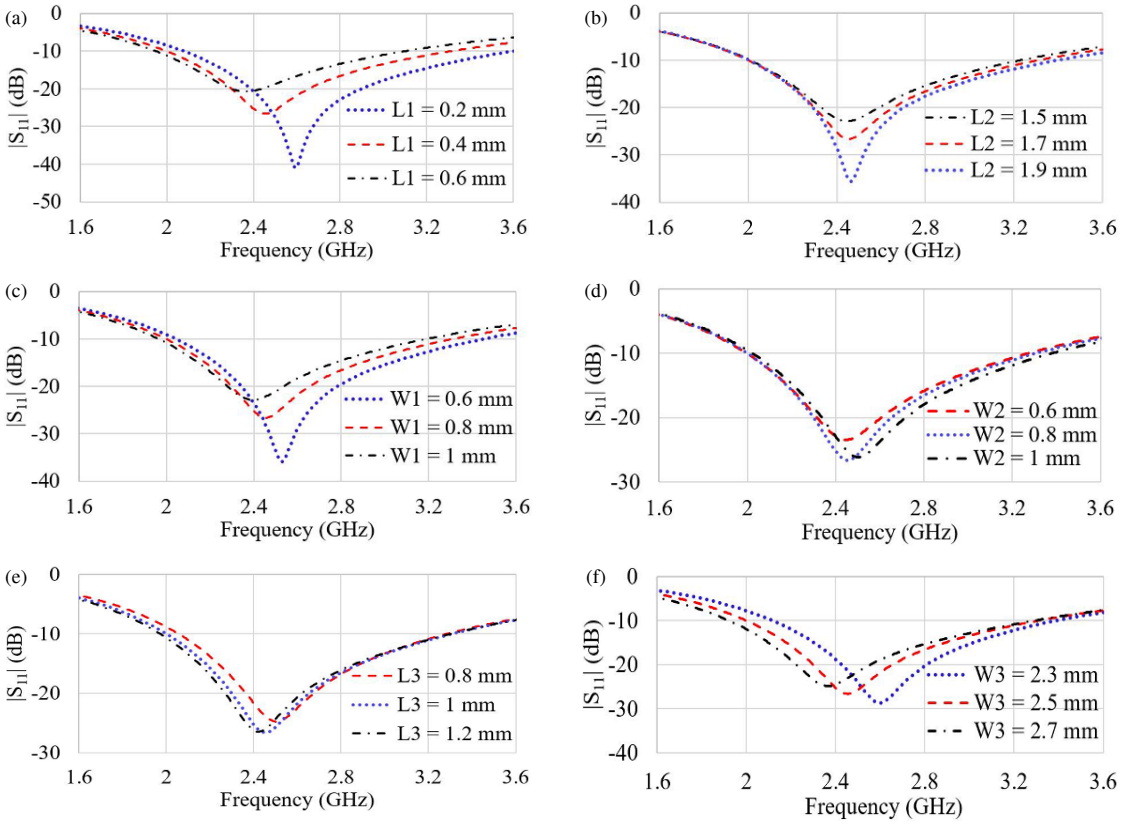

FIGURE 13. Parametric study of key design parameters for the proposed antenna.

As shown in Figs. 13(e)–(f), the length (L_3) and width (W_3) of the DGS were independently varied. The results show that changes in the DGS length result in negligible shifts in resonance frequencies, with return losses remaining closely matched. In contrast, variations in the DGS width significantly affect the resonance behavior. However, due to the antenna's wide impedance bandwidth, the resonant frequencies still fall within the 2.4–2.48 GHz ISM band. This highlights the critical role of DGS width in tuning the antenna's response and emphasizes the antenna's tolerance to dimensional variations while maintaining robust performance.

3.1.6. Surface-Current and Power Analysis

The surface current distribution of the proposed implantable antenna at 2.45 GHz is analyzed. Fig. 14(a) represents the patch layer, showing a strong concentration of surface currents around the left and right-side arms, indicating active radiating elements contributing to magnetic field generation. Fig. 14(b) depicts the ground plane, where circular current flow is also observed, supporting the formation of magnetic fields that are essential for near-field communication. Additionally, elevated current densities are observed around the shorting pin regions, in both the patch and ground layers. Although only the implantable antenna was designed in this work, the observed current patterns suggest that the structure supports efficient magnetic field generation, making it a promising candidate for inductively coupled NFC-based biomedical communication systems. The dominant loop-like currents on both the patch and ground layers are characteristic of inductive behavior, which is favorable for magnetic coupling with an external wearable reader placed close to the skin surface.

To illustrate the operating principle of the proposed skin-implantable antenna, the power flow was simulated by analyzing the Poynting vector distribution. The Poynting vector

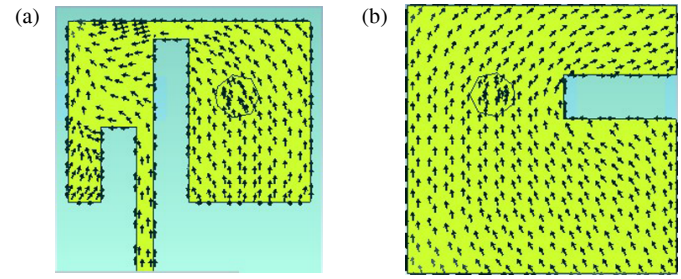

FIGURE 14. Surface current distributions of the proposed antenna on (a) the patch and (b) the ground.

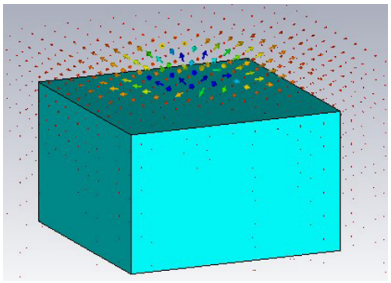

FIGURE 15. Spatial distribution of the Poynting vector above the skin surface.

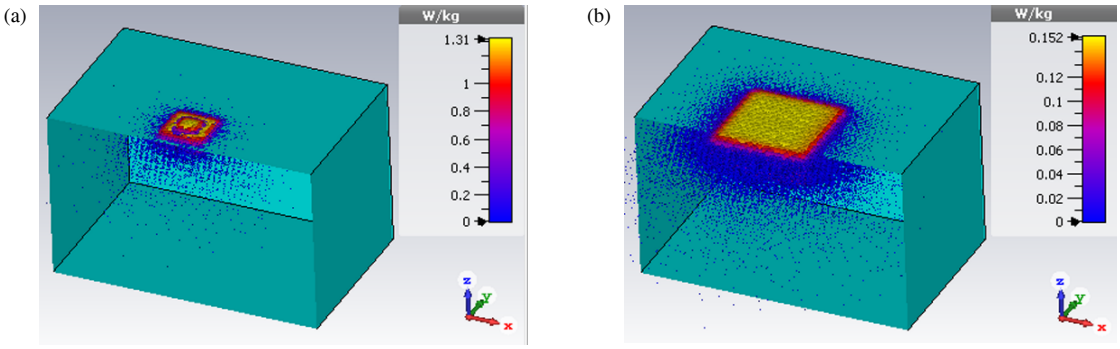

FIGURE 16. Specific absorption rate (SAR) analysis based on (a) 1-g and (b) 10-g averaging standards.

($\vec{S} = \vec{E} \times \vec{H}$) quantifies the electromagnetic (EM) power per unit area, where $\vec{E}$ and $\vec{H}$ represent the electric and magnetic field vectors, respectively. This vector is used to evaluate the direction and magnitude of EM energy propagation within the biological environment. Fig. 15 depicts the Poynting vector distribution at 2.45 GHz when the antenna is implanted 4 mm beneath the skin surface. As observed, the EM energy predominantly flows outward from the implant site toward the on-body receiver antenna positioned outside the tissue. This directional energy distribution confirms effective radiation through the skin interface, validating the antenna's suitability for near-field biomedical telemetry.

3.1.7. Analysis of Specific Absorption Rate (SAR)

Specific Absorption Rate (SAR) analysis was initially performed using an input power of 1 W to evaluate the worst-case electromagnetic exposure scenario. At this power level, the simulated SAR values reached 622 W/kg for the 1 g averaging mass and 92 W/kg for the 10 g averaging mass, significantly exceeding the maximum permissible limits defined by IEEE C95.1 (1.6 W/kg for the 1 g tissue standard) and ICNIRP (2.0 W/kg for the 10 g tissue standard) for localized tissue exposure [35]. To ensure compliance with these regulatory thresholds, the input power was proportionally scaled down based on the SAR-to-power ratio obtained from the initial simulation. A revised input power of 2 mW was identified as sufficient to maintain SAR values within the allowable limits. Subsequent simulations at this reduced power level yielded SAR values of 1.32 W/kg and 0.152 W/kg averaged over 1 g and 10 g of tissue, respectively, both well within the specified safety margins for implantable devices, as shown in Figs. 16(a)–(b). These results confirm the antenna's compliance with electromagnetic exposure regulations for short-range inductive coupling scenarios typical in NFC-based biomedical telemetry systems.

3.2. Antenna Fabrication and Measurements

Although the proposed antenna adopts a conventional inset-fed patch structure, it incorporates a strategically positioned shorting pin and an optimized defected ground structure (DGS) to achieve substantial miniaturization. This design leverages fundamental electromagnetic principles, such as current path elongation and inductive loading, while maintaining a simple layout. Compared to more intricate geometries, this approach reduces sensitivity to fabrication tolerances, thereby improving reproducibility and robustness. Figs. 17(a)–(b) show the pictorial view of the proposed antenna (patch and ground) fabricated using a traditional etching method with ferric chloride. Since the chosen substrate (FR-4) is very thin (0.36 mm), extra caution was required during the copper removal process to prevent damage to the patch and ground plane. The thin substrate makes the antenna appear nearly transparent from both sides. The patch and ground planes were electrically shorted using a copper wire, as specified by the design requirements. An SMA male connector was soldered to the antenna feed port to enable measurement and interfacing. Finally, biocompatible superstrates were attached on both sides of the antenna for protection and performance stability. Fig. 17(c) illustrates the polyamide superstrate ($\varepsilon_r = 4.3$, $\tan\delta = 0.004$) with a thickness of 0.05 mm, chosen for its excellent electrical insulation properties and suitability for high-temperature applications.

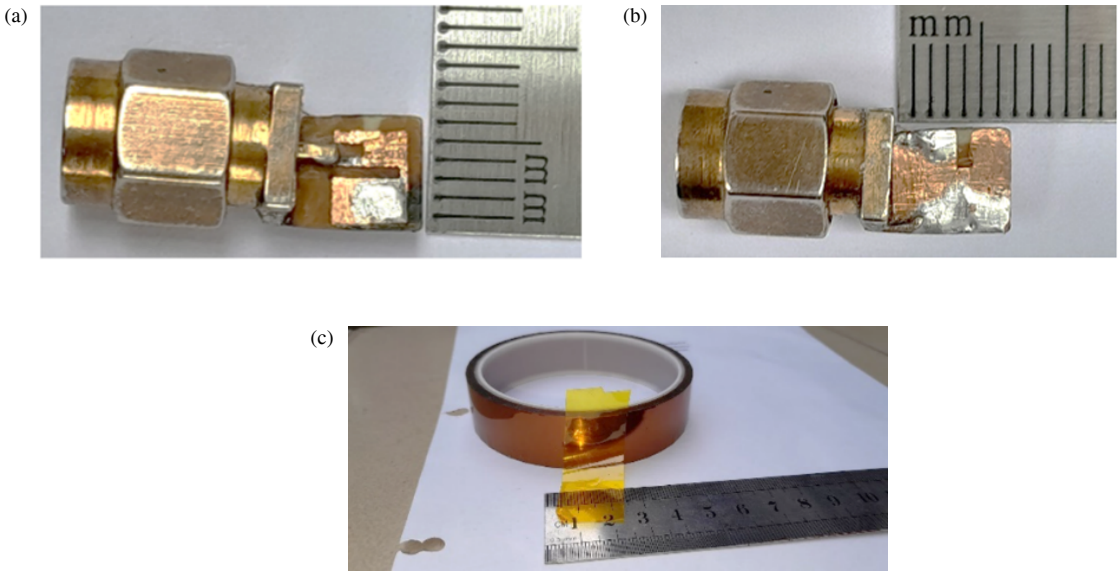

FIGURE 17. Prototype of antenna: (a) patch, (b) ground, and (c) polyamide insulator.

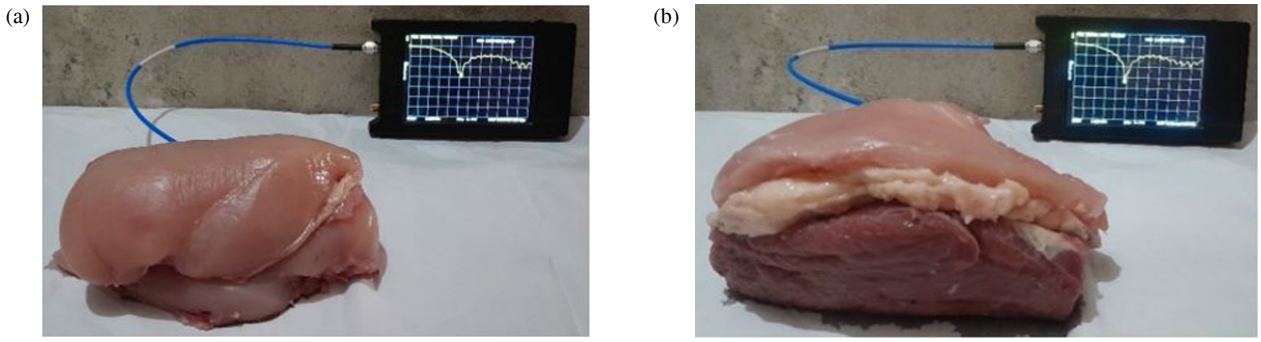

FIGURE 18. Measurement setup under (a) single-layer and (b) three-layer skin implant conditions.

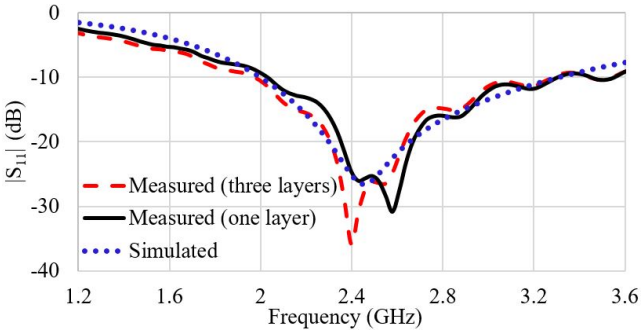

FIGURE 19. Simulated vs. measured $|S_{11}|$ response of the proposed antenna.

Antenna characterization under implantable conditions presents significant challenges. In vitro measurements often struggle to replicate the complex dielectric properties of biological tissues accurately, while ex vivo and in vivo measurements involve biological variability and material inconsistencies compared to actual human tissue. To address these limitations and simplify the study, ex vivo measurements were conducted with the antenna implanted at a depth of 4 mm under two different test setups, as shown in Figs. 18(a)–(b). In the first setup, illustrated in Fig. 18(a), chicken breast slabs were used to emulate a homogenous biological environment [9, 36]. To better approximate human tissue stratification, a second ex vivo setup was implemented using a three-layer tissue model, as depicted in Fig. 18(b). In this case, chicken breast was used to simulate skin, while the fat and muscle layers were harvested from a deceased cow [18]. The measurement results are shown in Fig. 19. In the first scenario, the antenna demonstrated a resonance frequency of 2.43 GHz with an $|S_{11}|$ of -26.04 dB, and the measured impedance bandwidth was 1290 MHz. Under the second scenario, the antenna achieved a resonance frequency of 2.40 GHz with an improved $|S_{11}|$ of -35.88 dB and a measured impedance bandwidth of 1260 MHz. For comparison, the simulated result in a skin-tissue phantom exhibited a resonance frequency of 2.45 GHz, $|S_{11}|$ of -26.59 dB, and -10 dB impedance bandwidth of 1280 MHz. The close agreement between the simulated and measured data confirms the proposed antenna's stable and reliable performance for near-field inductive coupling in biomedical telemetry applications.

4. CONCLUSION

This work has demonstrated the design and evaluation of a compact single-band implantable antenna tailored for Near-Field Communication (NFC) applications at 2.45 GHz. The antenna achieved substantial miniaturization by incorporating a shorting pin between the patch and ground plane, a defected ground structure (DGS), and leveraging the high dielectric properties of biological tissue. The final structure, with dimensions of $6 \times 6 \times 0.46\,\text{mm}^3$, exhibited near-optimal impedance matching of $51.14 + j4.6\Omega$ and achieved a -10 dB fractional bandwidth of 52.24%. Electromagnetic safety compliance was ensured by maintaining SAR levels at 1.32 W/kg and 0.152 W/kg averaged over 1 g and 10 g of tissue, respectively, well below the IEEE C95.1 and ICNIRP limits. Owing to the short-range nature of NFC systems, the design circumvents far-field gain constraints, making it well suited for efficient data telemetry and wireless power transfer. Ex vivo measurements conducted in chicken tissue confirmed the validity of the simulation results, reinforcing the antenna's robustness under realistic loading conditions. Overall, the proposed antenna provides a technically viable and biocompatible solution for energy-efficient, miniaturized implantable wireless systems operating in body-centric near-field environments.

REFERENCES

[1] Pournoori, N., L. Sydänheimo, Y. Rahmat-Samii, L. Ukkonen, and T. Björninen, "Small triple-band meandered pifa for brain-implantable biotelemetric systems: Development and testing in a liquid phantom," *International Journal of Antennas and Propagation*, Vol. 2021, No. 1, 6035169, 2021.

[2] Nguyen, D. and C. Seo, "An ultra-miniaturized circular polarized implantable antenna with gain enhancement by using DGS and holey superstrate for biomedical applications," *IEEE Access*, Vol. 11, 16 466–16 473, 2023.

[3] Shah, S. M. A., M. Zada, J. Nasir, H. Yoo, *et al.*, "Ultraminiaturized triband antenna with reduced SAR for skin and deep tissue implants," *IEEE Transactions on Antennas and Propagation*, Vol. 70, No. 9, 8518–8529, Sep. 2022.

[4] Kaim, V., B. K. Kanaujia, S. Kumar, H. C. Choi, K. W. Kim, and K. Rambabu, "Ultra-miniature circularly polarized CPW-fed implantable antenna design and its validation for biotelemetry applications," *Scientific Reports*, Vol. 10, No. 1, 6795, 2020.

[5] Singh, G. and J. Kaur, "Small footprint biocompatible antenna for implantable devices: Design, in-silico, in-vitro and ex-vivo testing," *Iranian Journal of Science and Technology, Transactions of Electrical Engineering*, Vol. 47, No. 3, 1145–1152, 2023.

[6] Pan, Y., W. Fu, D. Lu, T. Huang, Y. Song, L. Lu, and Y. Yan, "A compact impedance matching layer for dual-band implantable medical devices," *IEEE Antennas and Wireless Propagation Letters*, Vol. 23, No. 10, 3088–3092, Oct. 2024.

[7] Soliman, M. M., M. E. H. Chowdhury, A. Khandakar, M. T. Islam, Y. Qiblawey, F. Musharavati, and E. Z. Nezhad, "Review on medical implantable antenna technology and imminent research challenges," *Sensors*, Vol. 21, No. 9, 3163, 2021.

[8] Felício, J. M., C. A. Fernandes, and J. R. Costa, "Miniaturized implantable patch antenna for near-field communication at ISM band," in *2017 IEEE International Symposium on Antennas and Propagation & USNC/URSI National Radio Science Meeting*, 1685–1686, San Diego, CA, USA, 2017.

[9] Kamel, Y. A., H. A. Mohamed, H. ELsadek, and H. M. ELhennawy, "RF communication between dual band implantable and on body antennas for biotelemetry application," *Scientific Reports*, Vol. 15, No. 1, 4065, 2025.

[10] Javan-Khoshkholgh, A. and A. Farajidavar, "An implantable inductive near-field communication system with 64 channels for acquisition of gastrointestinal bioelectrical activity," *Sensors*, Vol. 19, No. 12, 2810, 2019.

[11] Berkelmann, L. and D. Manteuffel, "Antenna parameters for on-body communications with wearable and implantable antennas," *IEEE Transactions on Antennas and Propagation*, Vol. 69, No. 9, 5377–5387, Sep. 2021.

[12] Kirtania, S. G., A. W. Elger, M. R. Hasan, A. Wisniewska, K. Sekhar, T. Karacolak, and P. K. Sekhar, "Flexible antennas: A review," *Micromachines*, Vol. 11, No. 9, 847, 2020.

[13] Goswami, S. and D. C. Karia, "A metamaterial-inspired circularly polarized antenna for implantable applications," *Engineering Reports*, Vol. 2, No. 10, e12251, 2020.

[14] Abdi, A. and H. Aliakbarian, "A miniaturized UHF-band rectenna for power transmission to deep-body implantable devices," *IEEE Journal of Translational Engineering in Health and Medicine*, Vol. 7, 1–11, 2019.

[15] Mainul, E. A. and M. F. Hossain, "A metamaterial unit-cell based patch radiator for brain-machine interface technology," *Heliyon*, Vol. 10, No. 6, e27775, 2024.

[16] Fan, Y., Z. Li, X. Liu, X. Li, C. Xu, and H. Yang, "Compact triple-broadband implantable antenna for multi-functions in telemedicine," *IET Microwaves, Antennas & Propagation*, Vol. 16, No. 2-3, 153–162, 2022.

[17] Mainul, E. A. and M. F. Hossain, "A miniaturized triple band DGS implantable antenna for biotelemetry," in *2021 International Conference on Electrical, Communication, and Computer Engineering (ICECCE)*, 1–6, Kuala Lumpur, Malaysia, 2021.

[18] Zaki, A. Z. A., E. K. I. Hamad, T. G. Abouelnaga, H. A. Elsadek, S. A. Khaleel, A. J. A. Al-Gburi, and Z. Zakaria, "Design and modeling of ultra-compact wideband implantable antenna for wireless ISM band," *Bioengineering*, Vol. 10, No. 2, 216, 2023.

[19] Alamri, S., A. AlAmoudi, and R. Langley, "Gain enhancement of implanted antenna using lens and parasitic ring," *Electronics Letters*, Vol. 52, No. 10, 800–801, 2016.

[20] Zada, M., I. A. Shah, and H. Yoo, "Metamaterial-loaded compact high-gain dual-band circularly polarized implantable antenna system for multiple biomedical applications," *IEEE Transactions on Antennas and Propagation*, Vol. 68, No. 2, 1140–1144, 2019.

[21] Liu, K., Z. Li, W. Cui, K. Zhang, M. Wang, C. Fan, H. Zheng, and E. Li, "Investigation of conformal MIMO antenna for implantable devices based on theory of characteristic modes," *IEEE Transactions on Antennas and Propagation*, Vol. 70, No. 12, 11 324–11 334, 2022.

[22] Bahrouni, M., G. Houzet, T. P. Vuong, P. M. Mendes, H. Dinis, R. Silva, and H. Trabelsi, "Modeling of a compact, implantable, dual-band antenna for biomedical applications," *Electronics*, Vol. 12, No. 6, 1475, 2023.

[23] Butt, A. D., J. Khan, S. Ahmad, A. Ghaffar, A. J. A. Al-Gburi, and M. Hussein, "Single-fed broadband CPW-fed circularly polarized implantable antenna for sensing medical applications," *PLoS One*, Vol. 18, No. 4, e0280042, 2023.

[24] Janapala, D. K., N. Moses, and J. Bhagavathsingh, "Compact size antenna for skin implantable medical devices," *International Journal of Microwave and Wireless Technologies*, Vol. 16, No. 2, 217–226, 2024.

[25] Kumar, R. and S. Singh, "CPW-fed conformal PIFA design for implantable IoMT devices with wideband performance," *IEEE Sensors Journal*, Vol. 24, No. 1, 231–237, 2024.

[26] Kangeyan, R. and M. Karthikeyan, "Circularly polarized implantable MIMO antenna for skin, brain and heart implantation with wide axial ratio bandwidth," *International Journal of Communication Systems*, Vol. 37, No. 10, e5778, 2024.

[27] Iqbal, A., M. Al-Hasan, I. B. Mabrouk, and T. A. Denidni, "Self-quadruplexing antenna for scalp-implantable devices," *IEEE Transactions on Antennas and Propagation*, Vol. 72, No. 3, 2252–2260, 2024.

[28] Sihvola, A., *Electromagnetic Mixing Formulas and Applications*, IET, 1999.

[29] Edwards, T. C. and M. B. Steer, *Foundations of Interconnect and Microstrip Design*, Wiley Online Library, 2000.

[30] Shah, S. M. A., M. Zada, J. Nasir, O. Owais, and H. Yoo, "Electrically-small antenna with low SAR for scalp and deep tissue biomedical devices," *IEEE Access*, Vol. 10, 90 971–90 981, 2022.

[31] Alazemi, A. J. and A. Iqbal, "A compact and wideband MIMO antenna for high-data-rate biomedical ingestible capsules," *Scientific Reports*, Vol. 12, No. 1, 14290, 2022.

[32] Seidenari, S., G. Giusti, L. Bertoni, C. Magnoni, and G. Pellacani, "Thickness and echogenicity of the skin in children as assessed by 20-MHz ultrasound," *Dermatology*, Vol. 201, No. 3, 218–222, 2000.

[33] Farage, M. A., K. W. Miller, P. Elsner, and H. I. Maibach, "Characteristics of the aging skin," *Advances in Wound Care*, Vol. 2, No. 1, 5–10, 2013.

[34] Simić-Krstić, J. B., A. J. Kalauzi, S. N. Ribar, L. R. Matija, and G. N. Misevic, "Electrical properties of human skin as aging biomarkers," *Experimental Gerontology*, Vol. 57, 163–167, 2014.

[35] Lee, A.-K., S.-E. Hong, M. Taki, K. Wake, and H. D. Choi, "Comparison of different SAR limits in SAM phantom for mobile phone exposure," in *2018 Asia-Pacific Microwave Conference (APMC)*, 687–689, Kyoto, Japan, 2018.

[36] Das, S. and D. Mitra, "A compact wideband flexible implantable slot antenna design with enhanced gain," *IEEE Transactions on Antennas and Propagation*, Vol. 66, No. 8, 4309–4314, 2018.